Available online at www.sciencedirect.com
ScienceDirect
Journal of Computational Physics 227 (2008) 1643–1662
JOURNAL OF COMPUTATIONAL PHYSICS
www.elsevier.com/locate/jcp

# Implementation of nonreflecting boundary conditions for the nonlinear Euler equations

Oliver V. Atassi [a,*], José M. Galán [b]

[a] Aerodynamics, Pratt & Whitney, 400 Main Street, East Hartford, CT 06108, United States
[b] Escuela Superior de Ingenieros, Universidad de Sevilla, Camino de los, Descubrimientos s/n, E-41092 Sevilla, Spain

Received 15 January 2007; received in revised form 12 September 2007; accepted 18 September 2007
Available online 18 October 2007

**Abstract**

Computationally efficient nonreflecting boundary conditions are derived for the Euler equations with acoustic, entropic and vortical inflow disturbances. The formulation linearizes the Euler equations near the inlet/outlet boundaries and expands the solution in terms of Fourier–Bessel modes. This leads to an 'exact' nonreflecting boundary condition, local in space but nonlocal in time, for each Fourier–Bessel mode of the perturbation pressure. The perturbation velocity and density are then calculated using acoustic, entropic and vortical mode splitting. Extension of the boundary conditions to nonuniform swirling flows is presented for the narrow annulus limit which is relevant to many aeroacoustic problems. The boundary conditions are implemented for the nonlinear Euler equations which are solved in space using the finite volume approximation and integrated in time using a MacCormack scheme. Two test problems are carried out: propagation of acoustic waves in an annular duct and the scattering of a vortical wave by a cascade. Comparison between the present exact conditions and commonly used approximate local boundary conditions is made. Results show that, unlike the local boundary conditions whose accuracy depends on the group velocity of the scattered waves, the present conditions give accurate solutions for a range of problems that have a wide array of group velocities. Results also show that this approach leads to a significant savings in computational time and memory by obviating the need to store the pressure field and calculate the nonlocal convolution integral at each point in the inlet and exit boundaries.


*Keywords:* Nonreflecting boundary conditions; Euler equations; Aeroacoustics, waves, scattering

## 1. Introduction

Many unsteady compressible flow problems are characterized by unsteady nonlinear interactions in a finite source region and wave propagation in the outer region. Unsteady compressible flow calculations in infinite domains require boundary conditions to satisfy the causality condition that all waves are outgoing [1]. In external problems, acoustic waves propagate to the far-field, in a reference frame moving with the mean flow,

* Corresponding author. Tel.: +1 860 565 5755.
*E-mail address:* atassio@pweh.com (O.V. Atassi).

0021-9991/$ - see front matter © 2007 Elsevier Inc. All rights reserved.
doi:10.1016/j.jcp.2007.09.028

as nondispersive waves at the speed of sound. In this case, the Sommerfeld radiation condition can be generalized and local boundary conditions, which use local information in space and time, have been derived [2] for the wave equation using asymptotic solutions in the limit where the length scale of the source region is small relative to the distance to the outer boundary. When the flow domain is internal, such as in ducts and nozzles, interaction with the duct walls makes the propagation of acoustic waves more complex and nonlocal conditions in both space and time are required in order to obtain exact nonreflecting boundary conditions. While exact conditions have been derived [3], they require storing information over all of space and time and thus are impractical to implement. This has led to the general use of approximate local boundary conditions [4,5] which are only exact for one-dimensional flows. Moreover, the error introduced by the local boundary conditions is problem dependent and unknown since the error depends on the angle of propagation of the acoustic wave, which is not a priori known, relative to the boundary.

Much of the recent work on nonreflecting boundary conditions has concentrated on their formulation for different geometries and equally importantly their efficient implementation [6–10] to simple problems governed by the wave equation. The efficient implementation of nonlocal boundary conditions for internal problems is especially difficult because they are inherently nonlocal in both time and space. One approach to improve the efficiency of implementation is to utilize algorithms for the convolution integrals which appear and compress the nonlocality in time [9–11].

The focus of this paper is to use the physics of the problem to minimize the nonlocality in space. An exact nonreflecting boundary condition for the three-dimensional wave equation in a duct was derived in a recent paper [6] by expanding the solution in terms of the azimuthal and radial (Fourier–Bessel) modes. The resulting coefficient of each mode is governed by a one-dimensional wave equation which is local in space but nonlocal in time for each Fourier–Bessel mode. In ducts, due to phase cancellation, there are many modes which do not propagate to the inflow/outflow boundaries but are instead cut-off [12]. The effectiveness of the boundary conditions in the present paper relative to the traditional method, where the boundary condition is applied at each grid point in the computational boundary, is most significant when the number of modes needed to accurately represent the pressure field is much less than the number of grid points at the inflow/outflow boundaries. For example in aeroacoustics, a significant source of noise and vibration is produced by the interaction of wakes with structural struts and rotors. The resulting azimuthal wavenumbers that are produced are a linear combination of the number of rotors and stators whose counts are often quite different. As a result, relatively few acoustic modes propagate to the inflow/outflow boundaries. However, fine grids are still needed to resolve the wakes shed from the structural struts and rotors. In the present method the inflow/outflow boundary conditions are independent of the fine grid and can be implemented with a relatively small number of modes. Another example occurs in heated flows where the unsteady heat release generates sound waves which propagate to the far-field. In these problems it is experimentally observed [13] that the unsteadiness is dominated by relatively low frequencies where only the lowest order azimuthal modes can propagate to the far-field. The number of propagating modes is a small finite subset of all the modes and so accurate representation of the pressure is obtained using a small finite number of propagating and weakly decaying modes. Again fine grids are needed to accurately resolve the vortical and entropic disturbances induced by the heat addition. Thus, for these types of problems, avoiding the need to store information throughout the computational boundary will significantly reduce the computational time and memory requirements and make it possible to extend the formulation to nonlinear problems provided that strong nonlinear effects are confined to a finite inner region.

For turbomachinery applications, using a superposition of a small number of propagating and weakly decaying modes to construct exact solutions has been successfully applied to the linearized Euler equations in the frequency domain. Hall and Crawley [14] first used this approach by expanding the velocity and pressure field in terms of a small number of modes and Fang and Atassi [15] showed that only the pressure needs to be expanded in terms of modes to avoid difficulties with representing the wakes downstream of the cascade. These methods are appropriate for forced response problems where the equations in the entire flow domain are linear and the problem is dominated by a known characteristic frequency. In these applications the number of propagating acoustic modes is determined at the characteristic frequency. Then the number of evanescent modes used is determined when the energy content of the higher order acoustic modes in the numerical solution is small and the solution becomes independent of the number of modes used in the normal mode expan-

sion. This approach has also been extended to calculate the scattering of sound in three-dimensional flows [16] and in nonuniform swirling flows [17]. However, these methods are not appropriate for problems where nonlinearities occur within the flow domain.

The present paper implements nonreflecting boundary conditions in a finite volume discretization of the Euler equations. The main objectives of the paper are: (i) generalizing and implementing the nonlocal conditions derived for the wave equation in [6,8,10] to the Euler equations with incident vortical, acoustic and entropic disturbances at the inflow boundary, (ii) showing how these conditions can be extended to nonuniform internal flows, (iii) implementing the boundary conditions in a very efficient manner especially for problems characterized by low frequencies such as flutter, combustion instability, etc. where only a few Fourier–Bessel modes propagate to the inflow/outflow boundaries and (iv) assessing the impact of linearizing near the inflow/outflow boundaries, which introduces errors of the order of the square of the amplitude, by solving several computational examples from aeroacoustics with the nonlinear Euler equations.

In Section 2, the governing equations in the flow domain are presented. In Section 3, the nonreflecting boundary conditions are derived by linearizing the Euler equations about a uniform mean flow and it is shown how to extend them to problems where incident vorticity and pressure waves are imposed at the inlet of the domain. In Section 4, the inflow/outflow conditions are extended to swirling flows. In Section 5, the implementation of the conditions for the discretized equations is presented. In Section 6 results are presented for the propagation of acoustic waves and the scattering of a vortical wave by a cascade where accurate boundary conditions are needed to obtain high fidelity solutions. The effect of the number of modes used in the Fourier–Bessel expansion on the computational time and accuracy is also studied. The results are compared with the commonly used local boundary conditions of Thompson [4,5].

## 2. Governing equations in flow domain

We consider an inviscid nonheat conducting flow. The conservation equations for fluid motion in the volume, $\Omega$, bounded by the surface, $\partial\Omega$, are then expressed by

$$\frac{\partial}{\partial t}\int_{\Omega} W_{\mathrm{i}}\,\mathrm{d}\Omega + \int_{\partial\Omega} F^{\mathrm{C}}_{ij} n_j\,\mathrm{d}\Gamma = 0, \tag{1}$$

where $n_j$ is the unit normal of the surface $\partial\Omega$, the vector, $W_i$ and tensor, $F^{\mathrm{C}}_{ij}$, are the conservation variables and convective fluxes for mass, momentum and energy, respectively and are given explicitly in cartesian coordinates as

$$\begin{aligned} W_{\mathrm{i}} &= [\rho\ \rho u\ \rho v\ \rho w\ E]^{\mathrm{T}},\\ F_{ij} &= [\rho u_j\ p\delta_{1j} + \rho u u_j\ p\delta_{2j} + \rho v u_j\ p\delta_{3j} + \rho w u_j\ (E+p)u_j]^{\mathrm{T}}, \end{aligned} \tag{2}$$

where $\rho$ is the density, $u_j = [u\ v\ w]^{\mathrm{T}}$ are the cartesian components of the velocity field, $F_{ij}$ is the $j$th column of the $(5\times 3)$ matrix $F^{\mathrm{C}}_{ij}$, $p$ is the pressure and $E = \rho(c_v T + 1/2\sum_j u_j^2)$ is the total energy with, $T$, the temperature and $c_v$, the specific heat at constant volume.

In the test problems considered, the geometry is an annular duct whose inner and outer radii are $r = r_{\mathrm{h}}$ (hub) and $r = r_{\mathrm{t}}$ (tip), respectively. At the surface of the duct, $r = r_{\mathrm{h}}$, $r_{\mathrm{t}}$, and at any solid bodies which lie in the computational domain, the impermeability condition

$$u_j n_j = 0, \tag{3}$$

is locally applied.

We divide the domain into quadrilateral cells, fixed in time, by means of a structured mesh which is mapped into a rectangular grid with $i_{\max}$, $j_{\max}$ and $k_{\max}$ elements in each direction $i$, $j$ and $k$ through a bilinear mapping in each element. Taking $\vec{w}_{ijk}$ as the cell-averaged solution vector at the cell $(i,j,k)$, Eq. (1) can be written in semi-discrete form as

$$\frac{\mathrm{d}}{\mathrm{d}t}(\Omega_{ijk}\vec{w}_{ijk}) + \sum_{n=1}^{6}(\vec{F}^{\mathrm{C}})_n \delta\Gamma_n = 0, \tag{4}$$

where $\delta\Gamma_n$ is the area of the face $n$ and $\Omega_{ijk}$ is the volume of the cell. The solution is stored at the cell center and the fluxes are evaluated at the cell faces using second order accurate interpolation. The equations are then solved with second order accuracy in space and time using the MacCormack two-step predictor–corrector scheme. In what follows, we nondimensionalize the length, velocity and density with respect to $r_t$, the mean speed of sound, $c_0$, and the mean density, $\rho_0$, respectively.

## 3. Inflow/outflow boundary conditions for uniform mean flows

Inflow/Outflow boundary conditions are required which satisfy the physical causality condition at infinity to completely specify the problem. In order to specify an exact causality condition, solutions must be derived near the inflow/outflow boundaries which lie in the propagation region of the domain. In aeroacoustic applications the propagation region is characterized by small amplitude waves propagating in a nonuniform mean flow that is often swirling. In this section, we first derive nonreflecting boundary conditions for the Euler equations linearized about a uniform mean flow. In the next section, we extend these results and show the range of validity of the formulation for swirling flows.

We assume that the boundaries are located sufficiently far from the source region where nonlinear effects and vorticity are small such that the flow is approximated by the linearized Euler equations perturbed about a uniform mean flow. In this propagation region, $\Omega_p$, the flow variables are decomposed into a sum between their steady mean values and their unsteady disturbances,

$$\begin{aligned} &\mathbf{U} = \mathbf{U}_0 + \mathbf{u}(\mathbf{x},t), \quad \mathbf{x} \in \Omega_p, \\ &p = p_0 + p_1(\mathbf{x},t), \\ &\rho = \rho_0 + \rho_1(\mathbf{x},t) \end{aligned} \tag{5}$$

where $\mathbf{U}_0 = [M_x\ 0\ 0]^T$ is the mean velocity field, $M_x$ is the mean axial Mach number, $p_0 = 1/\gamma$ is the dimensionless mean pressure, $\rho_0 = 1$ is the dimensionless mean density and $\mathbf{u}$, $p_1(\mathbf{x},t)$, $\rho_1(\mathbf{x},t)$ are the unsteady velocity, pressure and density, respectively. The unsteady quantities are assumed small, i.e. $\{|\mathbf{u}|, |p_1|, |\rho_1|\} \ll \{M_x, p_0, \rho_0\}$.

The disturbances at the boundary are the sum of incident and scattered disturbances,

$$\mathbf{u} = \mathbf{u}_i + \mathbf{u}_s, \tag{6}$$

$$\rho_1 = \rho_i + \rho_s, \tag{7}$$

$$p_1 = p_i + p_s, \tag{8}$$

where the subscripts 'i' and 's' denote the prescribed incident and unknown scattered disturbances, respectively. For a uniform mean flow, we can split a general solution to the linearized Euler equations into independent acoustic, vortical and entropic disturbances. As a result, the velocity field may be decomposed into a convected solenoidal velocity field and an irrotational field [18] which produces pressure fluctuations but no entropy fluctuations. The pressure fluctuations are associated with the acoustic modes in the duct and they propagate with frequency dependent phase velocity due to reflections off the boundaries of the duct [12]. The vortical and entropic disturbances convect with the mean flow without producing a pressure field and the entropic disturbances only produce density fluctuations.

The acoustic disturbances are governed by the convective wave equation,

$$\left(\frac{D_0^2}{Dt^2} - \nabla^2\right) p_1(\mathbf{x},t) = 0, \quad \mathbf{x} \in \Omega_p, \tag{9}$$

where the convective derivative is defined,

$$\frac{D_0}{Dt} \equiv \frac{\partial}{\partial t} + M_x \frac{\partial}{\partial x}.$$

Once the pressure perturbation is known, the velocity and density are given by,

$$\frac{D_0 \mathbf{u}}{Dt} = -\nabla p_1 \tag{10}$$

and

$$\frac{\mathrm{D}_0\rho_1}{\mathrm{D}t} = \frac{\mathrm{D}_0 p_1}{\mathrm{D}t}, \tag{11}$$

respectively. Note the velocity field associated with the vortical disturbances is convected and satisfies (10) with the right hand side zero. In what follows, we derive nonreflecting boundary conditions at the inlet/exit of the computational domain from solutions to (9)–(11) in terms of the unknown variables $\mathbf{u}$, $p_1$, $\rho_1$ and an incident wave which is measured or specified as a function of time.

### 3.1. Outgoing solutions to the wave equation

Eq. (9) has two solutions: one which carries energy out of the flow domain and one which carries it into the flow domain. A nonreflecting boundary condition must then be applied so that only the outgoing solutions to (9) exist. Following [6], we assume $p_1(\mathbf{x},t)$ can be uniformly expanded in terms of the annular duct eigenfunctions,

$$p_1(x,r,\theta,t) = \sum_{n=1}^{n=\infty}\sum_{m=-\infty}^{m=\infty} p_{mn}(x,t)\mathrm{e}^{\mathrm{i}m\theta}R_{mn}(r), \tag{12}$$

where the Fourier–Bessel coefficient, $p_{mn}$, is given by

$$p_{mn}(x,t) = \frac{1}{2\pi\Lambda_{mn}}\int_{r_\mathrm{h}}^{1}\int_0^{2\pi} r\overline{R}_{mn}(r)\mathrm{e}^{-\mathrm{i}m\theta}p_1(x,r,\theta,t)\,\mathrm{d}\theta\,\mathrm{d}r, \tag{13}$$

where

$$\Lambda_{mn} = \int_{r_\mathrm{h}}^{1} r|R_{mn}|^2\,\mathrm{d}r$$

and the orthogonal eigenfunctions, $R_{mn}(r)$, are a combination of Hankel functions [1],

$$R_{mn}(r) = H_m^{(1)}(\lambda_{mn}r) - \frac{\mathrm{d}H_m^{(1)}(\lambda_{mn}r_\mathrm{h})/\mathrm{d}r}{\mathrm{d}H_m^{(2)}(\lambda_{mn}r_\mathrm{h})/\mathrm{d}r}H_m^{(2)}(\lambda_{mn}r), \tag{14}$$

where $\lambda_{mn}$ is the eigenvalue determined by the impermeability condition at the hub and tip of the annulus.

Following [6], we substitute (12) into (9) and Eq. (9) reduces to a one-dimensional wave equation for each mode,

$$\left[\frac{\mathrm{D}_0^2}{\mathrm{D}t^2} - \frac{\partial^2}{\partial x^2} + \lambda_{mn}^2\right]p_{mn}(x,t) = 0. \tag{15}$$

Using the Laplace transform results in two first order equations governing the downstream and upstream propagation of the wave,

$$\frac{\mathrm{d}\hat{p}_{mn}(x,s)}{\mathrm{d}x} + \frac{1}{\beta^2}\left((-M_x+1)s + \sqrt{s^2+\beta^2\lambda_{mn}^2} - s\right)\hat{p}_{mn} = 0, \tag{16}$$

$$\frac{\mathrm{d}\hat{p}_{mn}(x,s)}{\mathrm{d}x} - \frac{1}{\beta^2}\left((M_x+1)s + \left(\sqrt{s^2+\beta^2\lambda_{mn}^2} - s\right)\right)\hat{p}_{mn} = 0, \tag{17}$$

where $\beta$ is the Prandtl–Glauert factor, $\beta = \sqrt{1-M_x^2}$, and $\hat{p}_{mn}$ is the Laplace transform of $p_{mn}$ defined by,

$$\hat{p}_{mn}(x,s) \equiv \int_0^\infty \mathrm{e}^{-st}p_{mn}(x,t)\,\mathrm{d}t. \tag{18}$$

Both (16) and (17) can be solved by integrating with respect to $x$. Since $\sqrt{s^2+\lambda_{mn}^2\beta^2}$ is larger than $s$ finite solutions for $x\to\infty$ only exist for (16) and finite solutions for $x\to-\infty$ only exist for (17). Thus outgoing waves at the downstream boundary are governed by (16) and outgoing waves at the upstream boundary are governed by (17).

Applying the inverse Laplace transform to (16) and (17) each Fourier–Bessel mode must satisfy the relation

$$\int_0^t \left\{ \left( \frac{\partial p_{mn}}{\partial t'} \pm (1 \pm M_x) \frac{\partial p_{mn}}{\partial x} \right) J_0[\lambda_{mn}\beta(t-t')] + \frac{\lambda_{mn}}{\beta} p^{\pm}_{mn}(t')(1 \pm M_x) J_1[\lambda_{mn}\beta(t-t')] \right\} \mathrm{d}t' = 0. \tag{19}$$

The plus (minus) denotes a local nonreflecting condition at the outlet (inlet) of the domain for each Fourier–Bessel mode needed to accurately represent the pressure field at the computational boundaries. Since in many applications a small number of acoustic modes propagate only a few Fourier–Bessel coefficients need to be used. As a result, the condition, while nonlocal in time, is very efficient for time-dependent problems dominated by a few propagating acoustic modes.

The most commonly used boundary conditions are those based on the method of characterstics [4,5]. Thus, it is interesting to compare the present boundary conditions to the linearized characteristic boundary conditions. Summing over the Fourier–Bessel modes Eq. (19) can be written in the form,

$$\mathcal{L}^{\pm}_{NR} p_1 = \frac{\partial p_1}{\partial t} \pm (1 \pm M_x) \frac{\partial p_1}{\partial x} \mp (1 \pm M_x) \sum_m \sum_n \frac{\lambda_{mn}}{\beta} R_{mn}(r) \mathrm{e}^{\mathrm{i}m\theta} \int_0^t \left( \beta^2 \frac{\partial p_{mn}}{\partial x} - M_x \frac{\partial p_{mn}}{\partial t'} \right) J_1[(\lambda_{mn}\beta(t-t')] \, \mathrm{d}t' = 0. \tag{20}$$

This form enables a straightforward comparison with the method of characteristics, by taking the limit $\lambda_{mn} \to 0$. Moreover, it shows the error introduced by characteristic boundary conditions for higher order modes where $\lambda_{mn} \neq 0$. Note that this boundary condition reduces to $\frac{\partial p_1}{\partial x} = 0$ for a steady disturbance. Thus Eq. (20) can be written for the total pressure field $p$.

### 3.2. Boundary condition implementation for incident vortical and acoustic waves

In this subsection, we show the extension of Eq. (20) for problems with incident vortical and acoustic waves at the inlet. Eqs. (6)–(8) show that the disturbances can be decomposed into known incident and scattered disturbances. In a uniform flow, the acoustic, vortical and entropic disturbances are independent [18]. The vortical field is convected and pressure-free, the acoustic field is irrotational and the entropy field is a pure density fluctuation that convects with the mean flow. Thus substituting a pressure field, $p_{\mathrm{i}}$, associated with an incident acoustic wave into the boundary condition (20) yields,

$$\mathcal{L}^{-}_{NR} p_{\mathrm{i}} = \frac{2}{1+M_x} \frac{\partial p_{\mathrm{i}}}{\partial t}. \tag{21}$$

Note this relation eliminates the axial derivatives from (20) and only requires knowledge of the incident pressure at a single inlet plane.

In the present case, where we specify the incident disturbance at the inlet, the perturbation pressure is the sum of the incident and the outgoing scattered disturbances. The nonreflecting boundary condition must be applied on the outgoing pressure field, $p_{\mathrm{s}} = p_1 - p_{\mathrm{i}}$. Thus, the inlet pressure boundary condition (20) in terms of the perturbation pressure at the inlet is then

$$\mathcal{L}^{-}_{NR} p_1 = \frac{2}{1+M_x} \frac{\partial p_{\mathrm{i}}}{\partial t}. \tag{22}$$

At the exit, we do not, in this paper, specify an incident acoustic disturbance, i.e. $p_1 = p_{\mathrm{s}}$, and thus the nonreflecting condition takes the form,

$$\mathcal{L}^{+}_{NR} p_1 = 0. \tag{23}$$

It is convenient to use Eq. (20) to obtain an exact relation for the axial velocity at the inlet,

$$p_1 + u_x = (1 - M_x) \sum_m \sum_n R_{mn}(r) \mathrm{e}^{\mathrm{i}m\theta} \frac{\lambda_{mn}}{\beta} \int_0^t \{ (u_{x_{mn_{\mathrm{s}}}}(t') + M_x p_{mn_{\mathrm{s}}}) J_1[\lambda_{mn}\beta(t-t')] \} \, \mathrm{d}t' + p_{\mathrm{i}} + u_{x_{\mathrm{i}}} \tag{24}$$

where $u_{x_{\mathrm{s}}}, p_{\mathrm{s}}$ are the scattered axial velocity and pressure perturbations, respectively.

To obtain the axial velocity field at the exit of the computational domain, we discretize the axial component of (10) where the pressure is given by (23). The circumferential and radial velocity are also determined from the linearized momentum equation

$$\frac{D_0 u_\theta}{Dt} = -\frac{1}{r}\frac{\partial p}{\partial \theta}, \tag{25}$$

$$\frac{D_0 u_r}{Dt} = -\frac{\partial p}{\partial r}. \tag{26}$$

At the inlet, however, it is necessary to eliminate the axial derivatives to avoid downwinding the convective terms. Since the scattered field is irrotational, we can replace the axial derivatives in (25) and (26) by using the relations

$$\frac{\partial u_\theta}{\partial x} = \frac{1}{r}\frac{\partial u_x}{\partial \theta} - \frac{1}{M}\frac{\partial u_\theta^g}{\partial t} + \frac{1}{r}\frac{\partial u_\theta^g}{\partial \theta}, \tag{27}$$

$$\frac{\partial u_r}{\partial x} = \frac{\partial u_x}{\partial r} - \frac{1}{M}\frac{\partial u_r^g}{\partial t} + \frac{1}{r}\frac{\partial u_r^g}{\partial \theta}, \tag{28}$$

where $u_\theta^g, u_r^g$ are the circumferential and radial components of the incident vortical disturbance respectively. Finally, the density is related to the pressure by Eq. (11). At the inlet, this relation simplifies to $p_1^s = \rho_1^s$ for the outgoing pressure wave.

In Section 5, the nonlocal boundary conditions for the inflow and outflow boundaries are implemented. We denote BC1 as the nonlocal boundary conditions at the inflow and outflow boundaries consisting of Eqs. (11), (22), (24), (27) and (28) at the inlet and Eqs. (11) and (23) at the exit. To test the implementation of the nonlocal boundary condition, we compare its performance, in Section 6.1, to an inlet boundary condition, BC2, which consists of imposing the incident disturbance at the inlet and using Eqs. (11) and (23) at the exit. This boundary condition is exact when there are no reflected waves inside the domain. We also implement a local boundary condition, which is denoted by BC3, by taking $\lambda_{mn} = 0$ in relations (22) and (24) at the inlet and Eq. (23) at the exit.

## 4. Inflow/outflow boundary conditions for nonuniform potential mean flows

The mean flow in many internal flows such as those with turbomachinery contains swirl. As a result, even in the propagation region, the mean flow is not uniform. In this section, we extend the applicability of the methodology described above to swirling turbomachinery flows. The propagation of disturbances in a nonuniform fully developed flow has been examined in [19–21] and the disturbances are governed by a nonconstant coefficient wave equation for the potential. Moreover, recent work [22–24] on the propagation of potential disturbances has shown that this model can also be easily extended to incorporate the effect of slow changes in the area of the duct in the high frequency limit. In what follows, we start with a potential mean flow and determine the conditions where the exact nonreflecting boundary conditions derived for a uniform mean flow can be extended to swirling flows. In the propagation region, $\Omega_p$, the flow variables are decomposed into a sum between their steady mean values and their unsteady disturbances,

$$\mathbf{U} = \mathbf{U}_0(\mathbf{x}) + \mathbf{u}(\mathbf{x}, t), \tag{29}$$

$$p = p_0(\mathbf{x}) + p_1(\mathbf{x}, t), \tag{30}$$

$$\rho = \rho_0(\mathbf{x}) + \rho_1(\mathbf{x}, t). \tag{31}$$

The potential mean flow is assumed to vary only with $r$ and is of the form,

$$\mathbf{U}_0 = U_x(r)\mathbf{e}_\mathbf{x} + U_\theta(r)\mathbf{e}_\theta, \tag{32}$$

where $\mathbf{e}_x$ and $\mathbf{e}_\theta$ are the unit vectors in the axial and azimuthal directions, respectively for the velocity field.

The potential velocity field, $\phi(\mathbf{x}, t)$, for small-amplitude acoustic disturbances is governed by the convective wave equation [19],

$$\mathcal{L}\phi = 0, \quad \mathbf{x} \in \Omega_p, \tag{33}$$

where

$$\mathcal{L} \equiv \frac{1}{c_0^2}\frac{\mathrm{D}_0^2}{\mathrm{D}t^2} - \frac{1}{\rho_0}\nabla\cdot(\rho_0\nabla), \tag{34}$$

where the convective derivative is defined,

$$\frac{\mathrm{D}_0}{\mathrm{D}t} \equiv \frac{\partial}{\partial t} + \mathbf{U_0}\cdot\nabla.$$

The pressure is related to the potential function by

$$p_1 = -\rho_0\frac{\mathrm{D}_0}{\mathrm{D}t}\phi. \tag{35}$$

### 4.1. Narrow annulus limit

In many compressor and turbine stages, the hub-tip ratio is small, suggesting that the propagation of acoustic waves in swirling flow governed by (33) can be simplified. We consider the limit, $(r_\mathrm{t} - r_\mathrm{h})r_m \to 0$, where $r_m = 0.5\,(r_\mathrm{t} + r_\mathrm{h})$, while $(r_\mathrm{t} - r_\mathrm{h})$ remains finite and introduce $y = \frac{r - r_\mathrm{h}}{r_\mathrm{t} - r_\mathrm{h}}$. Substituting the eigenexpansion in Eq. (12) into Eqs. (34) and (35) and neglecting terms of $O(1/r_m)$ yields the following eigenvalue problem for the radial eigenfunctions,

$$\frac{\mathrm{d}^2 R_{mn}}{\mathrm{d}y^2} + (r_\mathrm{t} - r_\mathrm{h})^2\left(\lambda_{mn}^2 - \frac{m^2}{r_m^2}\right)R_{mn} = 0, \tag{36}$$

and the impermeability condition at the hub and tip of the duct. Note $\lambda_{mn}$ is the eigenvalue and $m$ can be large such that $\frac{m(r_\mathrm{t} - r_\mathrm{h})}{r_m} = O(1)$.

The radial eigenfunction and eigenvalues have the solution,

$$\begin{aligned} R_{mn}(y) &= \cos(n\pi y),\\ \lambda_{mn} &= \sqrt{\frac{n^2\pi^2}{(r_\mathrm{t} - r_\mathrm{h})^2} + \frac{m^2}{r_m^2}}. \end{aligned} \tag{37}$$

The propagation of waves can then be reduced to a constant coefficient wave equation. As in Section 3, we transform the convective wave equation for each Fourier–Bessel component to obtain two ordinary differential equations governing the waves with upstream and downstream going group velocities, respectively:

$$\frac{\mathrm{d}\hat{p}_{mn}(x,s)}{\mathrm{d}x} + \frac{1}{\beta^2}\left[-M_x\left(\frac{s}{c_0} + \mathrm{i}m\frac{M_\theta}{r_m}\right) + \sqrt{\left(\frac{s}{c_0} + \mathrm{i}m\frac{M_\theta}{r_m}\right)^2 + \beta^2\lambda_{mn}^2}\right]\hat{p}_{mn} = 0, \tag{38}$$

$$\frac{\mathrm{d}\hat{p}_{mn}(x,s)}{\mathrm{d}x} - \frac{1}{\beta^2}\left[M_x\left(\frac{s}{c_0} + \mathrm{i}m\frac{M_\theta}{r_m}\right) + \sqrt{\left(\frac{s}{c_0} + \mathrm{i}m\frac{M_\theta}{r_m}\right)^2 + \beta^2\lambda_{mn}^2}\right]\hat{p}_{mn} = 0 \tag{39}$$

where $\hat{p}_{mn}$ is the Laplace transform of $p_{mn}$, $M_x(r_m)$, $M_\theta(r_m)$ and $\beta = 1 - M_x^2$ is the Prandtl–Glauert factor. Using the Convolution theorem to take the inverse Laplace transform yields the nonreflecting boundary conditions,

$$\int_0^t \mathrm{e}^{-\mathrm{i}m\frac{U_\theta}{r_m}(t-t')}\left\{\left(\frac{1}{c_0}\frac{\partial p_{mn}}{\partial t} \pm (1 \pm M_x)\frac{\partial p_{mn}}{\partial x}\right)J_0[\lambda_{mn}c_0\beta(t-t')] + \frac{\lambda_{mn}(1 \pm M_x)p_{mn}}{\beta}J_1[\lambda_{mn}\beta(t-t')]\right\}\mathrm{d}t' = 0$$

where the plus (minus) denotes the nonreflecting condition at the outlet (inlet) of the domain and $\lambda_{mn}$ is given by (37). Note that this equation is similar to that of the uniform flow relation, (19), except for the Doppler shift resulting from the mean flow swirl.

## 5. Numerical implementation of the boundary conditions

In this section, we present the numerical implementation of the wall boundary condition, the periodicity condition and the inflow/outflow implementation. Several model problems are solved in Section 6 which utilize these boundary conditions.

### 5.1. Wall boundary conditions

The impermeability condition at the solid boundaries (hub, tip, vanes) implies that the velocity normal to the wall vanishes. Thus, the convective flux at the wall is left with the pressure terms only. The required value of the pressure at the wall is obtained with a 3-point one-sided scheme, which for a uniform grid is given by

$$p_{\mathrm{w}} = \frac{1}{8}(15p_1 - 10p_2 + 3p_3), \tag{41}$$

where the subindex $i = 1, 2, 3$ indicates the relative cell position with respect to the wall along the normal direction (1 being the closest and 3 the furthest).

### 5.2. Periodicity condition

In the $\theta$ direction the computational domain covers the range $[0, \theta_{\max}]$. When the entire annulus is considered, $\theta_{\max} = 2\pi$, a periodic boundary condition is applied without a loss of generality. For the case of wake interaction with a flat plate cascade, considered in Section 6.2, the periodic condition is applied upstream and downstream of the leading and trailing edges, respectively. If we wish to validate our calculation against linear solutions, small-amplitude disturbances are imposed at the inlet and a reduction in the azimuthal size of the domain can be obtained by using a quasi-periodic boundary condition over a sector. In what follows, a periodic or quasi-periodic boundary condition is applied to relate the disturbances at both ends

$$\mathbf{Y}(x, \theta_{\max}, r, t) = \mathbf{Y}(x, 0, r, t)\mathrm{e}^{\mathrm{i}\sigma}, \tag{42}$$

where $\mathbf{Y} = [\rho_1, u_x, u_\theta, u_r, p_1]^{\mathrm{T}}$ are the primitive variables in cylindrical coordinates, $\sigma = m\theta_{\max}$ and $m$ is the circumferential wavenumber. For the particular case where $\sigma$ is $2\pi$ multiplied by an integer number, a periodic condition occurs: $\mathbf{Y}(x, \theta_{\max}, r, t) = \mathbf{Y}(x, 0, r, t)$.

### 5.3. Inflow/outflow implementation

Both the Fourier–Bessel coefficients and the nonlocal convolution integral must be approximated to implement the inflow/outflow boundary conditions. In what follows, we present the implementation used to approximate these integrals. Eq. (13) gives the relationship to determine the Fourier–Bessel coefficient in terms of the pressure perturbation. In a finite volume scheme, the pressure is evaluated at the midpoint of the volume making the midpoint rule a very convenient method of integration. We approximate the Fourier–Bessel coefficients by

$$p_{mn}(x, t) = \sum_{j=1}^{N_{th}} \sum_{k=1}^{N_r} \Delta r_{jk} \Delta\theta_{jk} p_1(r^*_{jk}, \theta^*_{jk}, x, t)\mathrm{e}^{-\mathrm{i}m\theta^*_{jk}} \overline{R}_{mn}(r^*_{jk}), \tag{43}$$

where $r^*_{jk}, \theta^*_{jk}$ are the coordinate locations at the midpoint of a cell volume.

For implementation, the form of the nonreflecting boundary conditions (19) is convenient for implementation because it does not require computing the Fourier–Bessel coefficients at several axial grid locations to calculate the convolution integrals. Instead, using the trapezoidal rule and summing over the modes Eq. (19) at time $t = t_k$ takes the approximated form,

$$\left(\frac{\partial p_1^k}{\partial t} \pm (1 \pm M_x)\frac{\partial p_1^k}{\partial x}\right) = -\sum_m \sum_n R_{mn}(r) e^{im\theta}\left(\kappa_{mn}^{k-1} + \sum_{p=1}^{k-2}(\kappa_{mn}^{p} + \kappa_{mn}^{p+1})\right), \tag{44}$$

where the kernel, $\kappa_{mn}^p = \left(\frac{\partial p_{mn}^p}{\partial t'} \pm (1 \pm M_x)\frac{\partial p_{mn}^p}{\partial x}\right) J_0[\lambda_{mn}\beta(t_k - t'_p)] + \frac{\lambda_{mn}}{\beta} p_{mn}^{\pm}(1 \pm M_x) J_1[\lambda_{mn}\beta(t_k - t'_p)]$. The axial derivative of the pressure in the nonreflecting boundary conditions (22)–(24) is evaluated using second order accurate one-sided differences.

## 6. Numerical results

In this section, we examine the performance of the inflow/outflow boundary conditions on several test cases to study the effectiveness of the nonlocal nonreflecting boundary condition implementation. The first case computes the transmission and reflection at the inflow and outflow boundaries of sound waves in an annular duct. This problem is ideal for assessing the error introduced by the inflow/outflow boundary conditions since the solutions can be compared against normal mode solutions for a given frequency and azimuthal wavenumber. Moreover, we focus on the propagation of low order azimuthal modes ($m = -2, -1, 0, 1, 2$) which characterize the acoustic field of heated flows such as those which occur in combustors and augmentors of aeroengines. Sensitivity of the solutions to the number of modes used in the Fourier–Bessel expansion and the size of the computational domain is also tested and results are compared against the local boundary conditions obtained in the limit $\lambda_{mn} \to 0$. The second test case calculates the scattering of a fan wake by a cascade of flat plate stator vanes. This is a problem of great practical interest in aeronautics and it is ideally suited for the boundary conditions presented here because the number of fan blades and stator vanes are often quite different resulting in a small finite number of circumferential modes which propagate to the far-field. This problem is also an interesting test of the boundary conditions because, in addition to the scattering of the wake into different acoustic modes, in the linear inviscid limit a vortex sheet (velocity discontinuity) lies downstream of the plate and the leading edge pressure has a square root singularity. As a result, this case also requires the outflow boundary condition to handle regions of strong vorticity which convect downstream of the flat plate and must pass through the outflow boundary without reflection.

### 6.1. Multi-dimensional wave propagation in uniform mean flows

An annular duct with hub-tip ratio $r_h/r_t = 0.5$ and a uniform mean flow Mach number, $M_x = 0.5$ is chosen. A time-harmonic disturbance which is a normal mode of the duct is imposed at the inflow boundary and the propagation of the multi-dimensional acoustic wave is calculated. Ideally, the acoustic wave should propagate downstream with zero reflections and its long-time solution should approach the time-harmonic normal mode solution [6].

The normal mode solution of the acoustic disturbance is given by

$$\mathbf{Y}_i = \mathbf{A}(r) e^{i(m\theta + k_{mn}^+ x - \tilde{\omega}t)}, \tag{45}$$

where the circumferential wavenumber $m$, radial mode order $n$, frequency $\tilde{\omega}$ are inputs and $\mathbf{Y}_i = [\rho_i, u_{x_i}, u_{\theta_i}, u_{r_i}, p_i]^T$. The axial wavenumber is given by

$$k_{mn}^{\pm} = \frac{-M_x\tilde{\omega} \pm \sqrt{\tilde{\omega}^2 - (1 - M_x^2)\lambda_{mn}^2}}{1 - M_x^2}, \tag{46}$$

where $+(-)$ indicates modes propagating with a group velocity downstream (upstream). Note the phase velocity is a function of frequency. The amplitude of the incident wave is

$$\mathbf{A}^T = a_{i,a}\left[R_{mn}, \frac{k_{mn}^+}{\tilde{\omega} - M_x k_{mn}^+}R_{mn}, \frac{m}{r(\tilde{\omega} - M_x k_{mn}^+)}R_{mn}, \frac{-i}{\tilde{\omega} - M_x k_{mn}^+}R'_{mn}, R_{mn}\right] \tag{47}$$

with $R'_{mn}(r) = \frac{dR_{mn}(r)}{dr}$ and $a_{i,a}$ a constant factor. Local conditions perform well when $\lambda_{mn}/\tilde{\omega}$ is small and poorly when $\lambda_{mn}/\tilde{\omega}$ is close to one. Note from (47) that the amplitudes of the velocity and density are dependent on

the incident pressure. The relations are determined from the momentum equation and the isentropic relation between the pressure and density perturbation.

*6.1.1. Propagation of different duct modes*

To test the performance of the boundary conditions over a range of phase speeds we compute the propagation of acoustic waves for several values of the reduced frequency, $\tilde{\omega} = \omega r_m/c_0 = 0.4\pi, \pi, 2\pi, 4\pi$. The azimuthal wavenumber is $m = -1$ for these cases. Note that for the two highest frequencies there are two and three propagating modes, respectively. In these cases, $\tilde{\omega} = 2\pi, 4\pi$, we input the second ($n = 2$) and third ($n = 3$) radial modes, respectively, to see the accuracy with which higher order modes are calculated. The three propagating radial eigenfunctions of the incident mode, $R_{mn}(r)$, and their derivatives, $R'_{mn}(r)$, are plotted in Fig. 1. For the two low frequencies $\tilde{\omega} = 0.4\pi, \pi$ only one acoustic mode propagates and the eigenfunction is denoted by the circles. When the frequency increases to $\tilde{\omega} = 2\pi$ a second propagating mode occurs which is denoted in the figure by the pluses and whose eigenfunction crosses the radial axis once. For $\tilde{\omega} = 4\pi$, a third mode propagates with even larger radial variation which is denoted by the triangle symbols. Thus each frequency, $\tilde{\omega} = 0.4\pi, \pi, 2\pi, 4\pi$ contains modes which propagate with different phase velocities and their corresponding values of $\lambda_{mn}/\omega$ are 0.81, 0.32, 0.78 and 0.76, respectively. Note that the eigenfunctions cross the radial axis one and two times for the incident waves of the two cases corresponding to $\tilde{\omega} = 2\pi, 4\pi$, respectively.

The amplitude of the incident wave is chosen to be small, $a_{i,a} = 0.001$, to obtain an almost linear solution which can be compared with the known analytical solution of the linearized Euler equations. The size of the domain in the $x$ and $\theta$ directions is 0.1 and $2\pi$, respectively. A dense uniform grid, shown in the title of Fig. 2, is used to separate the error at the boundary from the truncation error of the finite volume scheme. A periodic condition is applied in the $\theta$ direction and a CFL number of $1/(1 + M_x)$ is used.

In what follows, we compare the numerical results with three different sets of boundary conditions at the inlet and exit boundaries. The first two boundary conditions, BC1 and BC2, are both nonlocal and nonreflecting. BC1 corresponds to using the nonlocal boundary conditions presented in Section 3 at both the inlet and exit whereas BC2 applies the same nonreflecting boundary condition at the exit but at the inlet the following incident normal mode in (47) is enforced: $\mathbf{W} = \mathbf{W}_i = [1 + \rho_i,\ (1 + \rho_i) \cdot (M_x + u_i), (1 + \rho_i)v_i, (1 + \rho_i)w_i, E_i]^{\mathrm{T}}$ at $x = x_{\mathrm{inlet}}$. Note that the five variables are not imposed independently but rather are obtained from the incident

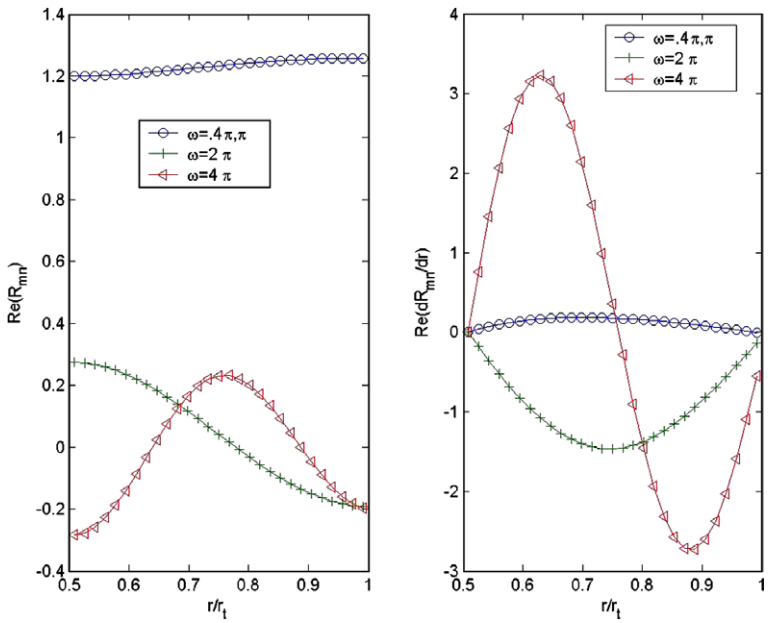


Fig. 1. Radial eigenfunction (left) and its derivative (right) of the incident acoustic mode at several values of the reduced frequency $\tilde{\omega} = \omega r_m/c_0 : 0.4\pi, \pi, 2\pi, 4\pi$.

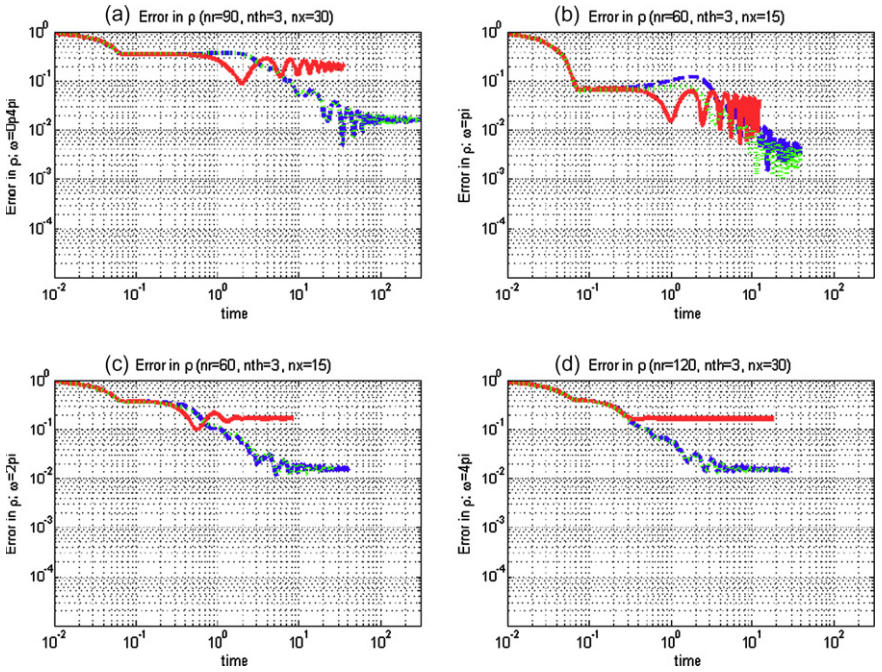


Fig. 2. Propagation of an incident acoustic wave at several values of the reduced frequency $\tilde{\omega}$: (a) $0.4\pi$, (b) $\pi$, (c) $2\pi$, (d) $4\pi$. The relative error in $\rho_1$ for the solutions obtained with boundary conditions BC1, BC2 and BC3 is plotted versus time with thin-dashed, thick-dashed and thick-dashed lines, respectively.

pressure field, $p_i$. For example, the velocity perturbations are related to the pressure through the linear momentum equation, (10). This condition amounts to imposing that the nonincident field is zero which is appropriate in this case but in the general case where scattering occurs, such as in fan wake stator interaction, this condition is highly reflective. The purpose of comparing BC1 and BC2 is to assess the performance of the numerical implementation at the inflow boundary which requires taking information from inside the computational domain (downstream) and must be done carefully to avoid numerical instabilities [25]. The third boundary condition, BC3, uses a local boundary condition at the exit, where $\lambda_{mn} = 0$ in (19) and (23), while imposing the known incident disturbance at the inlet as in BC2.

The convergence of the solutions using the three sets of boundary conditions are presented in Fig. 2 with thin-dashed (BC1), thick-dashed (BC2) and thick-continuous lines (BC3), respectively. The number of grid points used in each coordinate direction, $(x, \theta, r)$ is indicated in the title of each subplot. The average error at any time step $t$ is calculated as

$$e = \frac{1}{n_{\text{cells}}|a_{i,a}|} \sum_{i=1}^{i_{\max}} \sum_{j=1}^{j_{\max}} \sum_{k=1}^{k_{\max}} |\rho_{1,ijk} - \rho_{1,ijk}^{\text{exact}}| \tag{48}$$

with $n_{\text{cells}} = i_{\max} \cdot j_{\max} \cdot k_{\max}$. To obtain a relative measure of the convergence we divide the average error by the average error at the first time step $t = \mathrm{d}t$. Note that since this test problem depends on a single frequency and the average error involves the magnitude of the difference between the density and the exact normal mode solution the average error should not vary in time once the solution has reached a time-periodic solution.

For large $t$, the error, as expected, for the two nonlocal exact conditions BC1 and BC2 is very similar, while for the local condition, BC3, it is always much higher. The errors in the converged solution obtained with BC3 at all frequencies are approximately 20.0%, 2.8%, 17.3% an 17.0%, respectively, which are approximately 13, 9, 11 and 12 times higher than the errors obtained with the nonlocal condition BC1 and its subset BC2. The worst case, shown in the top row of the first column, for the local boundary condition corresponds to the lowest frequency $\tilde{\omega} = 0.4\pi$, where the ratio $\lambda_{mn}/\omega$ is closest to unity. Even in the best case, $\tilde{\omega} = \pi$, where the error with the local condition is small due to the low value of $\lambda_{mn}/\omega$, the error is still much higher than that of the

nonlocal boundary conditions. The excellent agreement between the two exact boundary conditions, BC1 and BC2, shows that the numerical implementation of the inflow boundary is working and provides comparable results to imposing the exact solution at the inflow boundary as is done in BC2.

Note that the convergence of the numerical solution to a time-periodic state with the nonlocal boundary conditions, shown in Fig. 2, is slower for the lowest frequency when compared with the higher frequencies. For that reduced frequency, $\tilde{\omega}$

resolve at the inflow/outflow boundary. Then the dispersion relation, Eq. (46), is used to determine the number of propagating acoustic modes. After this estimate, we gradually increase the number of modes until the solution is independent of the number of modes used, i.e. the solution content of the higher order modes is negligible.

To check the influence of the number of duct modes retained in the expansion and the resulting increase in computational time, we increase the number of radial, $n = N_n$, and circumferential modes, $m = N_m$, used in the Fourier–Bessel representation of the pressure field. For this study, we input a single incident wave with one zero crossing, $N_n = 2$, with reduced frequency $\tilde{\omega} = 2\pi$ and examine the sensitivity of the numerical solution with the general inflow/outflow implementation, BC2, to the number of terms used in the Fourier–Bessel expansion. In the case considered here only the $N_n = 2$, $m = -1$ mode should exist in the solution and any content in the other radial or circumferential modes is a result of error in the numerical solution.

The results showing the relative error of the solution are presented in Fig. 4. Recall that all of the higher order radial modes, $N_n > 2$, are exponentially decaying modes. Fig. 4 shows that increasing $N_m$ and $N_n$ does not modify the convergence of the numerical solution. A slight difference in the error is observed when 6 radial modes are used in the expansion. This occurs because the grid only contains 50 points in the radial direction and the error associated with the computation of the Fourier–Bessel coefficients is larger for the highest order radial modes, $n = 5, 6$.

The impact of the nonlocal boundary conditions and the number of modes used on the computational time is shown in Table 1. Four different cases were run with a single radial mode and different numbers of circumferential modes in the Fourier–Bessel expansion. The table gives the computational time needed to complete five time units from a given time $t_1$. In the table, the time, $\Delta T = \frac{T(t_1+5)-T(t_1)}{T(5)-T(0)}$, is normalized by the time it takes to go from $t = 0$ to $t = 5$ using a single Fourier–Bessel mode in BC2. For example, the first row shows that it takes 1.11 times longer with $N_m = 1$ and 2.10 times longer with $N_m = 6$ to go from $t = 5$ to $t = 10$ than it does to go from $t = 0$ to $t = 5$ with $N_m = 1$. These results show the extent with which the nonlocal boundary conditions slow down the computation. The cost of evaluating the nonlocal boundary condition increases linearly with time and so as the computation continues the computation is slowed down due to the linear increase in

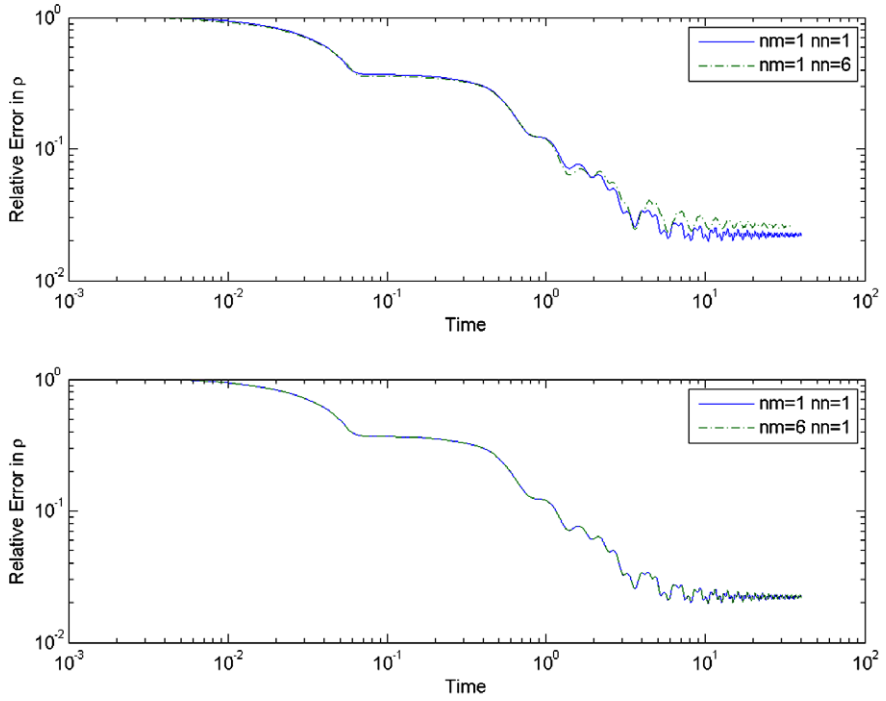


Fig. 4. Influence of the number of duct modes retained in the absorbing boundary conditions (22)–(24) at $\tilde{\omega} = 2\pi$. The relative error in $\rho_1$ obtained with BC2 is plotted in the following cases: (a) Top: $N_m = 1$ and $N_n = 1, 6$. (b) Bottom: $N_n = 1$ and $N_m = 1, 6$.

Table 1
Computational time increase due to nonlocal boundary conditions where $N_m$ refers to the number of circumferential modes used

| $\Delta T$ | $N_m = 1$ | $N_m = 2$ | $N_m = 4$ | $N_m = 6$ |
|---|---|---|---|---|
| $\frac{t(10)-t(5)}{t(5)}$ | 1.11 | 1.30 | 1.70 | 2.10 |
| $\frac{t(20)-t(15)}{t(5)}$ | 1.29 | 1.67 | 2.44 | 3.20 |
| $\frac{t(40)-t(35)}{t(5)}$ | 1.66 | 2.40 | 3.92 | 5.40 |
| $\frac{t(60)-t(55)}{t(5)}$ | 2.02 | 3.12 | 5.34 | 7.60 |

Only one radial mode, $N_n$, was used in each case.

time needed in evaluating the convolution integrals. For example even for $N_m = 1$, the time it takes to go from $t = 55$ to $t = 60$ is twice as long as it takes to go from $t = 0$ to $t = 5$. Furthermore, when there are 6 modes in the expansion it takes 7.60 times as long. These results illustrate the computational cost of using nonlocal boundary conditions and the importance of minimizing the number convolution integrals that are evaluated by minimizing the number of Fourier–Bessel modes.

In many applications where the frequencies are relatively low such as combustion generated noise, only a few low order azimuthal modes propagate in the duct. Motivated by this application, we impose four incident acoustic modes with azimuthal wavenumbers, $m = -1, 0, 1, 2$ and compute their transmission coefficients. The amplitudes of each of the incident modes are $a_{-11} = 1.0$, $a_{01} = 0.5$, $a_{11} = 0.33$ and $a_{21} = 0.25$, respectively where the first index denotes the azimuthal mode and the second the radial mode. The transmission coefficients normalized by the amplitude of the incident waves are shown in Table 2 and are all close to unity which denotes perfect transmission through the boundary.

### 6.1.3. Influence of domain size

Another means of assessing the nonreflecting boundary conditions is to ensure that the numerical solution is independent of the size of the domain. Three different meshes which only differ in their length in the axial direction: small ($\Delta x = 0.1$), medium ($\Delta x = 0.3$) and large ($\Delta x = 0.9$) are used to compute the propagation of the second radial acoustic mode with frequency, $\omega = 2\pi$ and amplitude, $a_{i,a} = .001$. The meshes are all uniform, with the same element size along the three cylindrical coordinates. A single mode is retained in the absorbing boundary conditions, and quasi-periodicity is used to reduce the computational domain to a single element in the $\theta$-direction.

Table 3 shows the amplitudes of the outgoing duct modes at the inlet and exit calculated with BC1 and BC3 normalized by the amplitude of the incident mode. The exact values should be unity at the exit boundary and zero at the inlet boundary. As expected the nonlocal boundary condition, BC1, at the inlet and exit of the domain yields a much more accurate solution than the local boundary condition, BC3. For example, the transmission coefficient at the exit is approximately 1.01 for the nonlocal boundary condition and is only *.83* using the local boundary condition. Both boundary conditions exhibit some sensitivity to the domain size at the inlet of the domain, however, the sensitivity falls within the error of the calculation and is relatively small.

Table 2
Amplitude of the transmitted acoustic mode at the exit for each propagating mode $m = -1, 0, 1, 2$, respectively

| $\lvert p^+_{-11}\rvert/\lvert a_{-11}\rvert$ | $\lvert p^+_{01}\rvert/\lvert a_{-01}\rvert$ | $\lvert p^+_{11}\rvert/\lvert a_{11}\rvert$ | $\lvert p^+_{21}\rvert/\lvert a_{21}\rvert$ |
|---|---|---|---|
| 1.014 | 1.009 | 1.014 | 1.01 |

Table 3
Amplitude of the transmitted acoustic mode at the inlet and exit for three different domain sizes

| Domain size | $\lvert p^+_{mn}\rvert/\lvert a_{i,a}\rvert$BC1 | $\lvert p^+_{mn}\rvert/\lvert a_{i,a}\rvert$BC3 | $\lvert p^-_{mn}\rvert/\lvert a_{i,a}\rvert$BC1 | $\lvert p^-_{mn}\rvert/\lvert a_{i,a}\rvert$BC3 |
|---|---|---|---|---|
| Small | 1.014 | 0.83 | .01 | 0.18 |
| Medium | 1.013 | 0.82 | .01 | 0.12 |
| Large | 1.013 | 0.82 | .01 | 0.18 |

### 6.2. Scattering of vortical waves by a flat plate cascade

An important problem in unsteady aerodynamics is the interaction of a wake from an upstream rotor with downstream structural vanes. When the airfoils are modeled as flat plates this problem can be compared against analytically based solutions which utilize the Wiener-Hopf technique [26,27]. This problem, in the inviscid limit, is characterized by a pressure field response to the incoming wake which, for high enough frequencies, produces outgoing acoustic waves at the inflow and outflow boundaries. The unsteady pressure field on the airfoil is dominated by a square root singularity at the leading edge of the plate. Downstream of the trailing edge lies a vortex sheet which convects with the mean flow velocity. These features make the problem a challenging one for computational methods and they also test the ability of the outflow boundary to transmit vortices and wakes without reflections. Often, in applications such as tonal fan noise, the number of blades in the fan is much smaller number than the number of vanes and, as a result, relatively few propagating modes are produced. Thus, the approach presented in this paper is ideal for this class of problems as well as relatively low frequency phenomena which occur in aeromechanical and combustion related applications.

The scattering of vortical waves by a flat plate cascade in a uniform flow is considered below. The case chosen corresponds to the problem proposed by Hanson as a CAA benchmark problem from the 3rd Computational Aeroacoustic Workshop [28] for rotor–stator interaction. In this problem, an annular cascade of 24 flat plate stator vanes, $N_v = 24$, is placed in a constant area annular duct. The constant chord, zero thickness vanes are parallel to the duct axis, and the ratio gap/chord at the tip is unity. The vortical gust is generated by an upstream rotor with 16 blades, $N_b = 16$, rotating at an angular speed $\Omega$, and it can be expressed in terms of harmonics of the blade passing frequency (BPF): $\omega_p = p \times \omega_{BPF}$, with $\omega_{BPF} = N_b\Omega$ and $p = 1, 2, \ldots$. In our calculations only the fundamental BPF, $p = 1$, is considered.

The wake is modeled as a harmonic excitation imposed at the inlet, $x = x_0$,

$$\begin{aligned} u_\theta &= M_x a \exp[\mathrm{i}(\omega_1 x_0/M_x + m\theta - \omega_1 t)], \\ u_r &= 0, \\ \nabla \cdot \mathbf{u} &= 0. \end{aligned} \tag{49}$$

When the wake interacts with the cascade of airfoils it scatters into disturbances with circumferential wavenumbers that satisfy the Tyler and Sofrin condition: $m = pN_b - j^*N_v$, with $j^* = \ldots -1, 0, 1, \ldots$, which in our case leads to $m = 16 - 24j^*$.

The numerical solution is compared with the 2-D Wiener-Hopf solutions of Glegg [26]. The output of interest in aeroacoustic applications is the amplitude of the outgoing acoustic waves at the inlet and exit boundaries of the computational domain. In order to compare with the 2-D solutions, we have studied the case of incident waves with no radial variation in a narrow annulus, $r_h/r_t = 0.98$. In this case, the scattering is limited to the azimuthal modes and the solution does not vary significantly in the radial direction. A small value is chosen for the amplitude of the incident wave, $a_{i,v} = 0.002$, to keep our full Euler solution within the linear regime.

The size of the computational domain in the $x$ and $\theta$ directions is $3b$ and $2\pi/N_v$, respectively, where $b = g_t$ is the chord length and $g_t = 2\pi r_t/N_v$ is the gap between vanes at the tip. A single passage of the cascade, between two adjacent vanes, is discretized. Quasi-periodic conditions are applied in the $\theta$ direction, as described in Section 5.1, with $\sigma = 2\pi\ m/N_v$. A uniform grid is used, and the number of nodes in each direction is $(n_x, n_\theta, n_r) = (281, 81, 3)$. The vanes are placed in the middle third of the computational domain in the $x$-direction, $x \in [b, 2b]$, and on the edges of the computational domain in the $\theta$-direction, $\theta = 0$ and $\theta = \frac{2\pi}{N_v}$. The general nonreflecting boundary condition, BC1, is used at the inlet and exit of the computational domain. A CFL number of approximately $1/(1 + M_x)$ is used.

Fig. 5 shows the amplitudes of each outgoing propagating mode at the reduced frequency of the harmonic excitation, $\tilde{\omega} = \Omega r_t/c_0$. For the time-dependent calculations, the amplitudes of the acoustic modes are time-dependent. An FFT over 20 periods of the excitation frequency is used to transfer the time-dependent solutions into the frequency domain. At the low frequencies, only one circumferential mode, $m = -8$, propagates. As the reduced frequency increases beyond fourteen a second mode, $m = 16$, propagates. Thus at these higher frequencies the energy of the incident wake scatters into both the $m = -8$ and the corotating $m = 16$ acoustic modes. The numerical solutions are compared with the analytic based solutions obtained using the Wiener-

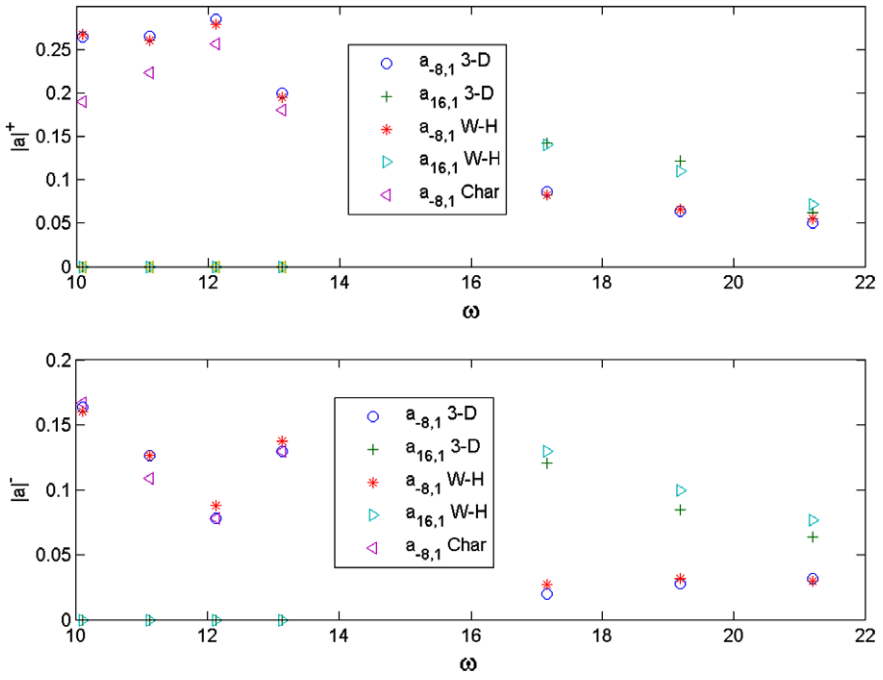


Fig. 5. Amplitudes of the outgoing acoustic modes are shown. The figure in the top row shows the amplitude of the outgoing modes at the exit boundary as a function of reduced frequency. The figure in the bottom row shows the amplitude of the outgoing modes at the inlet boundary as a function of reduced frequency. The circles and the plusses are the numerical solutions obtained with the nonreflecting boundary conditions, the stars and the right-pointing triangles are the Wiener-Hopf solutions, and the left-pointing triangles are the numerical results obtained with the local boundary conditions.

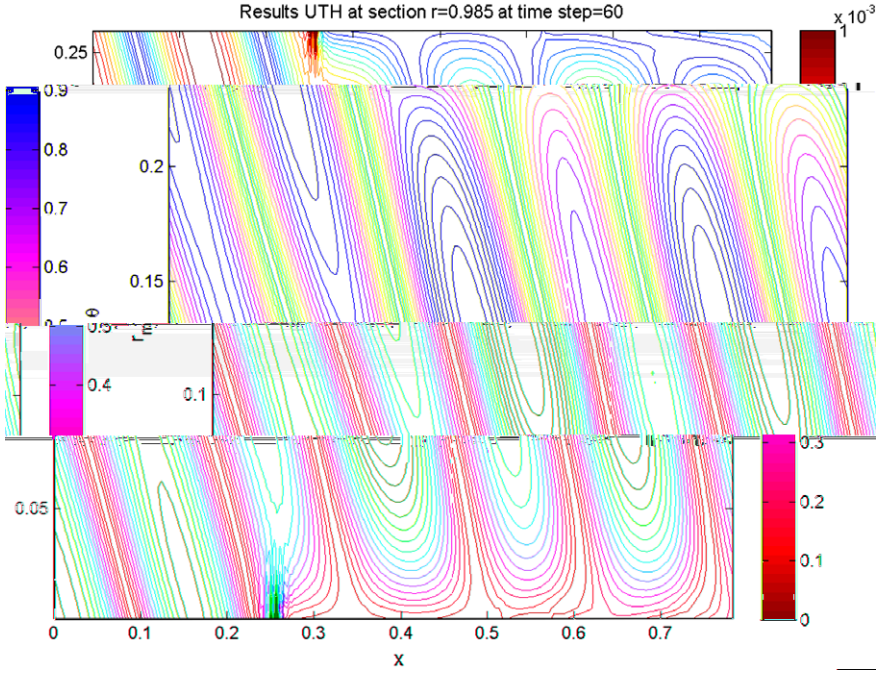


Fig. 6. Contour plot of the magnitude of $u_\theta$ in Fourier space on a surface $r =$ constant. The figure shows the scattering of a vortical gust by a cascade of flat plates in a narrow annular duct at $\tilde{\omega} = 11$. The abscissa is the $x$-axis and the ordinate is the coordinate $r_m\theta$ which shows a single passage of the cascade.

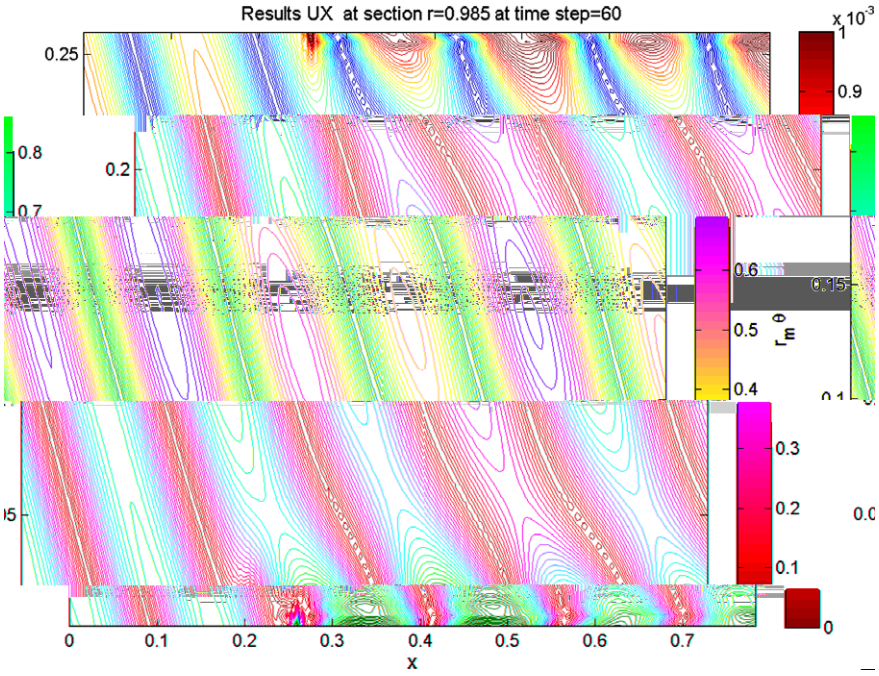


Fig. 7. Contour plot of the magnitude of $u_x$ in Fourier space on a surface $r =$ constant. The figure shows the scattering of a vortical gust by a cascade of flat plates in a narrow annular duct at $\bar{\omega} = 11$. The abscissa is the $x$-axis and the ordinate is the coordinate $r_m\theta$ which shows a single passage of the cascade.

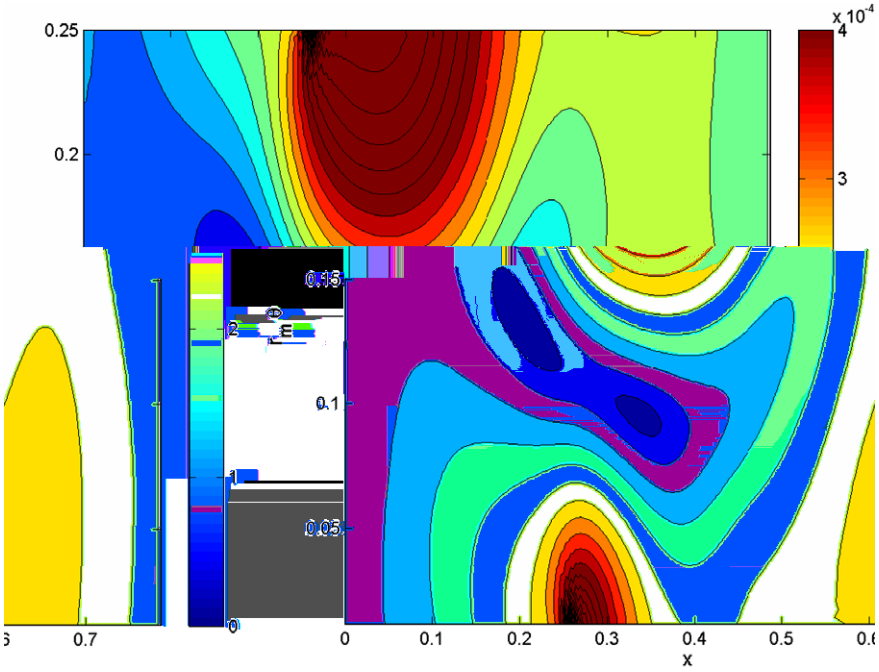


Fig. 8. Contour plot of the magnitude of pressure in Fourier space on a surface $r =$ constant. The figure shows the scattering of a vortical gust by a cascade of flat plates in a narrow annular duct at $\bar{\omega} = 11$.

Hopf technique. Comparison of the two solutions was facilitated by normalizing the pressure eigenfunctions so that their maximum values are equal to unity and for an upwash amplitude of $u_\theta^{(u)}$ equal to 0.1. The agreement with the 2D results is shown over a range of frequencies in Fig. 5.

The circles ($m = -8$) and the plusses ($m = 16$) denote the outgoing pressure amplitudes at the excitation frequency of the incident wake. Similarly, the stars ($m = -8$) and the right-pointing triangles ($m = 16$) denote the Wiener-Hopf solution for the outgoing pressure amplitudes for a given reduced frequency. The agreement between the two solutions is good over a range of frequencies. As the second mode cuts on most of the scattered acoustic energy downstream and upstream of the flat plate goes to the corotating, $m = 16$ mode. The left-pointing diamond shows the numerical solution using local boundary conditions for the pressure. The outgoing wave amplitudes are lower than the solution obtained with the nonlocal boundary condition and the Wiener-Hopf solution. This is likely due to increased reflections at the computational boundaries. The solution using the local boundary condition is worse at the exit than it is at the inlet since the orientation of the outgoing waves is closer to normal at the inlet than it is at the exit.

To examine the complete solution, we examine contour plots of the Fourier transformed velocity and pressure magnitudes for a particular case. Figs. 6–8 show contour plots of the Fourier transformed tangential velocity, axial velocity and pressure magnitudes respectively on a surface, $r =$ constant. In Fig. 6, the tangential velocity convects into the domain with a wavelength, $\lambda = U/f$ where $U$ is the mean velocity and f is the excitation frequency of the wake. Once the wake reaches the leading edge of the airfoil, $x = \pi/12$, the tangential velocity field adjusts to satisfy the impermeability condition on the surface of the flat plate, which lies between $\pi/12 \leqslant x \leqslant \pi/6$. Similarly, the axial velocity perturbation shown in Fig. 7 convects downstream and is cut by the flat plate. A region of high velocity gradient develops in the neighborhood of the flat plate which convects downstream through the outflow boundary of the computational domain. Fig. 8 shows the pressure magnitude which is produced by the interaction of the wake with the flat plate. The largest unsteady pressure occurs at the leading edge of the flat plate at the harmonic excitation frequency of the wake. Note that for a single mode, the magnitude of the pressure is constant. Near the inflow and outflow boundaries the magnitudes of the pressure become uniform and a single acoustic mode with azimuthal wavenumber, $m = -8$, propagates out of the computational inflow and outflow boundaries.

## 7. Conclusions

The nonlocal conditions derived for the wave equation in [6] have been generalized and implemented in a second order finite volume solution of the nonlinear Euler equations by linearizing near the inflow/outflow boundaries. While the exact nonreflecting boundary conditions are, in general, nonlocal in both space and time, one can often take advantage of the physics of the individual problem to minimize the computational time and memory required. For example, in many problems where the frequencies are low, such as flutter and combustion generated noise, or in rotor–stator interactions where the blade and vane counts are very different only a few propagating modes are needed to represent the pressure field away from the source region of the flow. To exploit this, the nonreflecting boundary conditions are expressed in Fourier space and lead to a local condition for each mode. When the number of modes needed to represent the acoustic pressure field is small compared to the computational grid, this approach should result in significant computational savings. This coupled with fast methods for evaluating the convolution integral [10,11] should make exact nonreflecting boundary conditions more widespread in real applications such as internal aerodynamics.

## Acknowledgements

The work was supported by the Ramon y Cajal Fellowship while the author was visiting the University of Seville. The author would like to thank Professor Antonio Barrero for the stimulating research environment during his stay at the University of Seville.

## References

[1] R. Courant, D. Hilbert, Methods in Mathematical Physics, John Wiley & Sons, 1937.
[2] A. Bayliss, E. Turkel, Radiation boundary conditions for wave-like equations, Comm. Pure Appl. Math. 33 (1980) 707–725.
[3] B. Engquist, A. Majda, Absorbing boundary conditions for the numerical simulation of waves, Math. Comp. 31 (1977) 629–651.

[4] K. Thompson, Time-dependent boundary conditions for hyperbolic systems, J. Comp. Phys. 68 (1987) 1–24.
[5] K. Thompson, Time-dependent boundary conditions for hyperbolic systems, II, J. Comp. Phys. 89 (1990) 439–461.
[6] O.V. Atassi, Nonreflecting boundary conditions for the time-dependent wave equation, J. Comp. Phys. 197 (2004) 737–758.
[7] M.J. Grote, J.B. Keller, Nonreflecting boundary conditions for time-dependent scattering, J. Comp. Phys. 127 (1996) 52–65.
[8] T. Hagstrom, Radiation boundary conditions for the numerical simulation of waves, Acta Numer. 8 (1999) 47–106.
[9] I.L. Sofronov, Non-reflecting inflow and outflow in a wind tunnel for transonic time-accurate simulation, J. Math. Anal. Appl. 221 (1998) 92–115.
[10] B. Alpert, L. Greengard, T. Hagstrom, Nonreflecting boundary conditions for the time-dependent wave equation, J. Comp. Phys. 180 (2002) 270–296.
[11] C. Lubich, A. Schadle, Fast convolution for nonreflecting boundary conditions, SIAM J. Sci. Comput. 24 (2002) 161–182.
[12] P.M. Morse, U.K. Ingard, Theoretical Acoustics, McGraw-Hill Inc., 1968.
[13] N.F. Mathews, D.C. Rekos, Prediction and measurement of direct combustion noise in turbopropulsion systems, J. Aircraft 14 (1977) 850–859.
[14] E.F. Hall, K.C. Crawley, Calculation of unsteady flows in turbomachinery using the linearized euler equations, AIAA J. 27 (1989) 777–787.
[15] J. Fang, H.M. Atassi, Numerical-solutions for unsteady subsonic vortical flows around loaded cascades, J. Turbomach.– Trans. ASME 4 (1991) 810–816.
[16] O.V. Atassi, A. Ali, Inflow/outflow conditions for internal time-harmonic Euler equations, J. Comp. Acoust. 10 (2002) 155–182.
[17] H.M. Atassi, A.A. Ali, O.V. Atassi, I.V. Vinogradov, Scattering of incident disturbances by an annular cascade in a swirling flow, J. Fluid Mech. 499 (2004) 111–138.
[18] L.S.G. Kovàsnznay, Turbulence in supersonic flow, J. Aero. Sci. 20 (1953) 657–682.
[19] V.V. Golubev, H.M. Atassi, Sound propagation in an annular duct with mean potential swirling flow, J. Sound Vibr. 198 (1996) 601–616.
[20] V.V. Golubev, H.M. Atassi, Acoustic-vorticity waves in swirling flows, J. Sound Vibr. 209 (1998) 203–222.
[21] O.V. Atassi, Computing the sound power in nonuniform flow, J. Sound Vibr. 266 (2003) 75–92.
[22] S.W. Rienstra, Sound transmission in slowly varying circular and annular lined ducts with flow, J. Fluid Mech. 380 (1999) 279–296.
[23] S.W. Rienstra, W. Eversman, A numerical comparison between multiple scales and finite-element solution for sound propagation in lined flow ducts, J. Fluid Mech. 437 (2001) 367–384.
[24] A.J. Cooper, N. Peake, Propagation of unsteady disturbances in a slowly varying duct with mean swirling flow, J. Fluid Mech. 445 (2001) 207–234.
[25] T. Hagstrom, H. Goodrich, Accurate radiation boundary conditions for the linearized euler equations in cartesian domains, SIAM J. Sci. Comput. 24 (2002) 770–795.
[26] S.A.L. Glegg, The response of a swept blade row to a three-dimensional gust, J. Sound Vibr. 227 (1999) 29–64.
[27] N. Peake, E.J. Kerschen, A uniform asymptotic approximation for high frequency unsteady cascade flow, Proc. Roy. Soc. London 449 (1995) 177–186.
[28] D.B. Hanson, Fan stator with harmonic excitation by rotor wake, in: 3rd CAA Workshop on Benchmark Problems, Category 4, 1999.